Failure of a pre-cracked epoxy sandwich layer in shear

S. Askarinejad[a], M. D. Thouless[b], N. A. Fleck[a]

[a]*Engineering Department, University of Cambridge, Cambridge, UK*
[b]*Department of Mechanical Engineering, University of Michigan, Ann Arbor, MI 48109, USA*

Abstract

Adhesive joints are frequently used in automotive, maritime and construction applications, yet joint reliability remains a concern. The purpose of this study is to develop a fracture mechanics methodology for the failure of an elastic-brittle lap-shear joint comprising a thick adhesive layer (an epoxy, of thickness on the order of 10 mm) sandwiched between thick steel adherends. This configuration is of practical application to ship-building, such as the bonding of a superstructure to the underlying hull. A modified thick-adherend shear test (TAST) is designed, and specimens are fabricated, with a range of interfacial pre-crack length and a range of adhesive layer thickness. The failure of samples with no pre-crack is governed by a critical value of corner singularity, whereas the failure of samples with long pre-cracks is governed by a critical value of interfacial stress intensity factor. Predictions for the dependence of failure load upon layer thickness and pre-crack length are obtained by analysing the elastic stress state for both a corner singularity and for an interfacial crack. Both the experimental results and the theoretical framework are useful in the design and fabrication of reliable lap-shear joints that comprise a thick elastic adhesive layer.

Keywords: Thick-adherend shear test, Adhesive, Fracture toughness, Corner singularity analysis

*Corresponding author
Email address: naf1@cam.ac.uk (N. A. Fleck)

1. Introduction

Historically, bolts and rivets are used to fasten assemblies of metallic and composite components. However, adhesively bonded joints offer benefits such as reduced weight and reduced through-life maintenance. Moreover, bonded joints obviate the need for holes associated with bolted joints, and hence reduce the number of stress raisers. Adhesive joints are under scrutiny for use in an increasing number of parts in aerospace and in marine structures, such as the joining of a steel-hulled ship to a composite superstructure (Maloney and Fleck, 2018; Saleh et al., 2020; Saeedifar et al., 2019). A major limitation in the use of adhesives for such applications is the lack of confidence in the reliability of adhesives by the Qualifying Agencies. An appropriate fracture mechanics methodology is also required. There has been some success in the use of the interfacial stress intensity factor for a bimaterial wedge (Gradin, 1982; Hattori et al., 1988) and a bimaterial butt joint (Reedy, 1993; Reedy and Guess, 1993, 1995, 1996) comprising a steel/epoxy interface. It remains a challenge to predict crack initiation from small pre-existing defects in the adhesive bondline such as porosity.

Commonly, the tensile peel strength of an adhesive layer is significantly below the shear strength, and consequently, the lap-shear joint is a preferred configuration in design (Possart and Brede, 2019; Bikerman, 2013). There is a need to develop predictive tools and test geometries for the failure of joints under macroscopic shear. Two classes of test exist for adhesives in shear: torsional shear and combined tension-shear. Torsional shear tests include the napkin ring test (ASTM E 229), and these have the advantage that they involve uniform shear loading, commonly that of simple shear. In contrast, tensile-shear geometries, such as single-lap shear test, double-lap shear test, Thick Adherend Shear Test (TAST) and the

butterfly test, exhibit non-uniform stress states, but are easier to perform and are usually more representative of practical joint geometries. The single-lap joint geometry inherently causes an eccentricity in the applied load path, leading to out-of-plane bending moments and to elevated peel stresses. This is particularly important in joints containing composite adherends due to their low strength in the through-thickness direction: peel stresses can lead to premature failure of the joint. The problem of eccentricity in loading is reduced in double-lap shear tests and in thick-adherend shear tests (TAST). There are many different types of TAST specimen based upon the work of Krieger (Krieger, 1975). Kassapoglou and Adelmann (Kassapoglou and Adelmann, 1992) investigated the effect of adhesive/substrate modulus mismatch on the adhesive shear distribution along the bond length in a TAST specimen, and concluded that decreasing modulus mismatch significantly increases the nonuniformity of shear stress distribution. Chiu and Jones (Chiu and Jones, 1992) investigated the effect of adhesive thickness on the shear stress and normal stress distributions within the TAST specimen, and highlighted the feature of a high tensile peel stress at the interface corners.

In the present study, a TAST specimen is used with pin loading, as shown in Fig. 1. The imposition of pin-loading, aligned with the mid-plane of the joint, prevents the development of an unknown bending moment and shear force at the ends of the specimen. One aim of the present study is to perform a detailed elastic singularity analysis of the TAST geometry of Fig. 1(a), with a pre-crack of length a present along the interface between adhesive and adherend. Note that a sharp corner exists at the end of the adhesive layer, and in the absence of a pre-crack, this 90° re-entrant corner leads to a local stress singularity from which cracks can initiate and grow. The addition of corner fillets diminishes this stress concentration, and may lead to an increased load carrying capacity of the joint (Lang and Mallick, 1998). A

literature has emerged on the role of corner singularities in dictating crack initiation. For example, Williams (Williams, 1952) investigated the effect of the boundary conditions on a quarter plane wedge upon the order of stress singularity. Bogy (Bogy, 1968, 1970) extended this study to the case of bonded quarter-planes. Subsequent studies have focused on corner singularities that arise in the butt joint geometry (Koguchi et al., 1996; Pageau and Biggers, 1995; Pageau et al., 1995).

A corner singularity, in the absence of macro defects such as a pre-crack, is characterised by the order of stress singularity (of value $\frac{1}{2}$ for the inverse square-root singularity at a conventional crack tip) and by the scalar magnitude of the singular stress field (analogous to the stress intensity factor for a conventional crack). Both the order of singularity λ and the magnitude H of singular stress field have been obtained for a number of joint geometries and loadings of practical importance, see for example (Munz and Yang, 1992; Ding et al., 1994; Akisanya and Fleck, 1997). It appears reasonable to assume that failure occurs when the imposed magnitude of singular stress field H attains a critical value H_c. This approach is analogous to linear elastic fracture mechanics, wherein failure occurs when the magnitude K of stress field attains the fracture toughness K_c. Recall that small scale yielding conditions prevail in linear elastic fracture mechanics when the size of plastic zone at the crack tip is much less than the domain of dominance of the elastic $K-$field. For the case of a corner singularity, the magnitude H of the corner singularity is a valid loading parameter provided the size of the plastic zone (and any fracture process zone) at the corner is much smaller than the domain of dominance of the singular stress field.

The aim of the present study is to measure, and to predict, the effect of adhesive layer thickness and pre-crack length upon the failure strength of a thick adherend shear test

(TAST) specimen comprising an elastic-brittle epoxy layer and steel adherends. A fracture mechanics methodology is developed in order to predict the failure load based on a minimum number of toughness parameters, with the corner singularity and the crack tip singularity for an interfacial crack both taken into account. First, a corner singularity analysis is used to account for the dependence of failure load upon layer thickness in samples absent a pre-crack. And second, the dependence of interfacial stress intensity factor and mode-mix upon pre-crack length and adhesive layer thickness are determined. By making use of both sets of analysis, we contrast crack initiation from the corner singularity with crack growth from a pre-existing crack.

2. Materials characterisation of the epoxy adhesive

A two-part, room-temperature curing epoxy adhesive was employed[1] due to its ability to form thick adhesive layers. The uniaxial tension response of the adhesive was measured by casting dogbone specimens from the adhesive; the dogbones are of gauge length 33 mm, width 6 mm, and thickness 3 mm. Wedge grips were used to grip the ends of the dogbone specimens in the screw-driven test machine; the axial strain over the gauge length was measured by a laser gauge and reflecting tabs on the specimen. Additionally, cube-shaped specimens, of side dimension 6 mm, were compressed between two smooth plates of the test machine in order to measure the uniaxial compressive response.

The nominal stress versus nominal strain response of the as-cured epoxy adhesive in uniaxial tension is given in Fig. 2(a) for three values of nominal strain rate $\dot{\varepsilon} = 1 \times 10^{-2} s^{-1}$,

[1]PRO-SET ADV-176/276 adhesive produced by Wessex Resins and Adhesives Limited, Romsey, UK

$2 \times 10^{-3} s^{-1}$ and $4 \times 10^{-4} s^{-1}$. Note that the ultimate tensile strength increases slightly from 32 MPa to 40 MPa and the nominal failure strain decreases slightly from 0.14 to 0.08, with increasing strain rate $\dot{\varepsilon}$. A similar sensitivity of nominal compressive strength to strain rate is evident in Fig. 2(b). True stress versus true strain responses under tension and compression, at a nominal strain rate of $\dot{\varepsilon} = 4 \times 10^{-4} s^{-1}$, are compared in Fig. 2(c). The small elevation in compressive strength over tensile strength is consistent with the well-established pressure-dependence of yield of polymers.

3. Fracture tests on TAST specimens

A series of fracture tests were performed on pre-cracked, modified Thick-Adherend Shear Test (TAST) specimens, recall Fig. 1(a). The thickness h of epoxy layer was varied from 3 mm to 13 mm, and the pre-crack length a was varied from 0 mm to 20 mm. In order to manufacture the modified TAST specimens, low carbon steel substrates were grit blasted and then degreased with acetone. The adhesive was applied (in accordance with the manufacturer's recommendations) using a manual applicator gun with a static-mixing nozzle. The adhesive layer thickness h was adjusted by shims. All specimens were cured at room temperature in ambient air for two weeks. Sharp pre-cracks were generated by razor tapping.

The tests on TAST specimens were conducted at a cross-head speed such that the average shear strain rate in the adhesive layer was $6 \times 10^{-4} s^{-1}$. A high resolution video was recorded at a rate of 0.2 frames per second to monitor the deformation of the adhesive. Digital Image Correlation (DIC) was employed to determine the shear strain distribution within the adhesive layer at all the stages of deformation. At least three specimens were tested for each crack length and layer thickness.

3.1. Mechanical response of TAST specimens

The average shear stress versus shear strain in the adhesive layer is shown in Fig. 3 for $a = 0$, $a = 10$ mm, and $a = 20$ mm. An elastic-brittle response is evident in each case, with the average shear strength decreasing with increasing h and with increasing a. In all cases, the failure mode was interfacial in nature, with no adhesive left on the substrate (not shown). The power law dependence of shear strength on adhesive layer thickness is different in specimens for which $a = 0$ (Fig. 4(a)) from that for specimens of pre-crack length $a = 10$ mm and $a = 20$ mm (Fig. 4(b)). Specifically, the failure strength scales as $h^{-0.35}$ in specimens with $a = 0$, and scales as $h^{-0.50}$ in specimens with $a = 10$ mm and $a = 20$ mm. An explanation for this behaviour is provided in the following sections.

4. Corner singularity analysis

Consider a TAST specimen with $a = 0$, and assume that a sharp 90° re-entrant corner exists at the junctions between the end face of the epoxy layer and the steel adherend. The presence of the 90° corner induces a singular stress field of the form discussed by Bogy (Bogy, 1970). Introduce a polar coordinate system (r, θ) centred on the corner such that $\theta = 0$ is along the layer/substrate interface, see Fig. 5(a). The asymptotic analysis of the stress field at the corner is detailed in Appendix A; it is found that a separation-of-variables solution exists for the stress such that the stress field σ_{ij} and displacement field u_i are of the form (Knésl et al., 2007)

$$\sigma_{ij} = H\, r^{\lambda-1}\, f_{ij}(\lambda, \theta) \tag{1}$$

and

$$u_i = H\ r^{\lambda}\ g_i(\lambda, \theta) \tag{2}$$

respectively, where λ is an eigenvalue, the parameter H is the intensity of loading, and f_{ij} and g_i are eigen-functions that capture the θ-dependence of the stress and displacement fields, respectively. Without loss of generality, we shall take $f_{22} = 1$. The details of the asymptotic analysis closely follow that of Khaderi et al. (Khaderi et al., 2015). The value of the eigenvalue λ and the eigenfield depend upon the degree of elastic mismatch between layer and substrate. Thus, upon specialising (1) to $\theta = 0$, the traction on the layer/substrate interface reads

$$\sigma_{12} = H\ r^{\lambda-1}\ f_{12}(\lambda, \theta = 0) \tag{3}$$

and

$$\sigma_{22} = H\ r^{\lambda-1}\ f_{22}(\lambda, \theta = 0) \tag{4}$$

Linearity and dimensional analysis dictate that the intensity of singularity H is related to the remote shear stress τ^{∞} and layer thickness h according to

$$H = \tau^{\infty}\ h^{1-\lambda}\ b(\alpha, \beta) \tag{5}$$

The value of $b(\alpha, \beta)$ is dependent upon specimen geometry and in the present study it is determined from a best fit of (4) to the traction distribution along the interface as $r \to 0$. The details are given below. The values of α and β quantify the mismatch in plane tensile

modulus across the interface, and the mismatch in the in-plane bulk modulus, respectively (Dundurs, 1969). In order to define them, label the layer above the interface (that is, the adhesive layer) as material $i = 1$ and the lower substrate (made from steel in the present experimental study) as material $i = 2$. Write μ_i as the shear modulus and ν_i as the Poisson ratio for material i. Then, for plane strain conditions, we have

$$\alpha = \frac{\mu_1 (1 - \nu_2) - \mu_2 (1 - \nu_1)}{\mu_1 (1 - \nu_2) + \mu_2 (1 - \nu_1)} \tag{6}$$

and

$$\beta = \frac{1}{2} \frac{\mu_1 (1 - 2\nu_2) - \mu_2 (1 - 2\nu_1)}{\mu_1 (1 - \nu_2) + \mu_2 (1 - \nu_1)} \tag{7}$$

We obtain $\alpha = -0.97$ and $\beta = -0.16$ upon taking ($E_2 = 200$ GPa, $\nu_2 = 0.30$) for the steel substrate, and ($E_1 = 2.20$ GPa, $\nu_1 = 0.40$) for the epoxy layer from references (Pandini and Pegoretti, 2008) and (Reedy and Guess, 1997), respectively. A strain-gauge rosette was placed within the gauge section of the tensile, dogbone specimen and confirmed that $\nu_1 = 0.40$ for the epoxy.

It is well-established (see for example, (Hutchinson and Suo, 1991)) that a non-vanishing value of β is associated with an oscillation in the stress and displacement fields near the tip of an interfacial crack. This leads to complications in the interpretation of mode-mix at an interfacial crack tip, as detailed later in this study. It is instructive to assume, as an alternative choice, that $\alpha = -0.97$ and $\beta = 0$, for example by taking $E_1 = 2.20$ GPa and $\nu_1 = 0.499$ for the epoxy layer. In this way, we can assess whether it is necessary to make use of the added complexity associated with a finite value of β in order to interpret the results.

The value of λ is determined by the eigenvalue analysis of Appendix A and is plotted in Fig. 6 as a function of α for the two choices $\beta = 0$ and $\beta = -0.16$. For the epoxy adhesive and steel combination ($\alpha = -0.97$) we find that $\lambda = 0.60$ for $\beta = 0$, and $\lambda = 0.65$ for $\beta = -0.16$. For comparison, recall that the singular stress field at the tip of a crack in an elastic solid scales as $r^{-\frac{1}{2}}$, implying $\lambda = 0.50$.

4.1. Finite element analysis

A series of finite element simulations using ABAQUS [2] were performed in order to verify the order of corner singularity for the modified TAST geometry and to obtain the calibration factor b in (5) for the relevant choice of geometry, $h/W = 0.10$. The two-dimensional finite element model consisted of the full TAST geometry, see Figs. 1 and 5(a). However, instead of pin loading, it was simpler and of acceptable accuracy to apply a uniform normal traction on the end faces of the steel substrates in order to generate the axial force F. A refined mesh was used in the vicinity of the interface corner such that the ratio of smallest element length to the adhesive layer thickness is 0.0002. Four-noded, bi-linear plane strain quadrilateral elements of reduced integration were employed. In addition, quadratic triangular elements (with 1/4 point nodes to capture the crack tip singularity) were placed at the crack tip when an interfacial crack was present.

The constant $b(\alpha, \beta)$ is determined by best-fitting (4) to the numerical results for $\sigma_{22}(r)$ as $r \to 0$ upon making use of the fact that $f_{22} = 1$. With this value of b, the asymptotic prediction (3) follows immediately. Take $\alpha = -0.97$, and let $\beta = 0$ and $\beta = -0.16$; the best fits of the asymptotic solution to the finite element solutions are given by $b = 1.47$

[2] Abaqus/Standard 2017. Dassault Systemes SIMULIA, Providence, Rhode Island.

and $b = 1.78$, respectively, for small values of r/h. Furthermore, the results for the shear stresses confirm that $f_{12} = 0.51$ and 0.42 for $\beta = 0$ and $\beta = -0.16$, respectively, as found in (Akisanya and Fleck, 1997; Khaderi et al., 2015). The FE predictions of Fig. 5 show that the slopes of the log-log plots of σ_{22} versus r, and σ_{12} versus r, agree with the value $(\lambda - 1)$ from the asymptotic solution. The asymptotic solution is dominant for $r/h < 0.1$; higher order terms in the asymptotic expression are needed to obtain agreement for $r/h > 0.1$. The size of the singular domain is consistent with that observed in other corner singularity studies (Reedy, 1993; Akisanya and Fleck, 1997).

We emphasize that one can interpret the parameter H as a loading parameter that quantifies the magnitude of the singular stress field at the interface-corner. When the value of H attains a critical value H_c fracture initiates, regardless of the details of non-linear deformation, damage and fracture within an embedded fracture process zone that is contained within the H-field. Thus, H plays a similar role for the initiation of fracture to the stress intensity factor K for the growth of a pre-existing crack. Upon adopting this interpretation for H the relation (5) suggests that the critical shear stress τ^{∞} for crack initiation from the interface-corner scales as $h^{(\lambda-1)}$. If we assume that $\lambda = 0.65$ for the choice $\beta = -0.16$ then we predict that τ_c^{∞} scales as $h^{-0.35}$ which is in excellent agreement with the observed scaling law of $\tau_c^{\infty} \propto h^{-0.35}$ in Fig. 4(a) for the case of a TAST specimen with no pre-crack present. Alternatively, if we assume that ν_1 for the adhesive equals 0.495 instead of 0.40, then we obtain ($\alpha = -0.97$, $\beta = 0$); consequently, λ equals 0.60 and the fracture strength τ_c^{∞} scales as $\tau_c^{\infty} \propto h^{-0.40}$ which deviates from the observed dependence of Fig. 4(a).

4.2. Analysis of interfacial crack

We proceed to analyse the case of an interfacial crack, of length a, on the lower interface of the adhesive layer. First, recall the definitions of the complex stress intensity factor K, the mode mix ψ and energy release rate G for an interfacial crack. The case of an interfacial crack embedded within the domain of dominance of the corner singularity is first considered, and then the general case of an interfacial crack that extends beyond the field of the corner singularity.

Recall that an oscillatory stress singularity exists at the tip of an interfacial crack when the Dundur's parameter β is non-vanishing. This is made clear from the traction distribution along the interface directly ahead of the crack (along $x_2 = 0$); it is of the form

$$\sigma_{22} + i\sigma_{12} = \frac{K}{\sqrt{2\pi x_1}}\, x_1^{i\epsilon} = \frac{K}{\sqrt{2\pi x_1}}\, e^{i\epsilon \ln x_1} \tag{8}$$

where $K = K_1 + iK_2$ is the complex intensity factor, with real part K_1 and imaginary part K_2. The oscillatory index ϵ is a function only of β such that

$$\epsilon = \frac{1}{2\pi}\ln\left(\frac{1-\beta}{1+\beta}\right) \tag{9}$$

Note that ϵ and the associated oscillations in the stress vanish when β vanishes. The ratio of shear traction σ_{12} to normal traction σ_{22} depends upon the distance x_1 ahead of the crack tip due to the presence of the $e^{i\epsilon \ln x_1}$ term in (8). Consequently, the mode mix ψ^* of an interfacial crack at an arbitrary distance ℓ ahead of the crack tip, is given by

$$\tan \psi^* = \frac{\sigma_{12}(x_1 = \ell)}{\sigma_{22}(x_1 = \ell)} = \frac{\mathrm{Im}(K\ell^{i\epsilon})}{\mathrm{Re}(K\ell^{i\epsilon})} \tag{10}$$

We note in passing that (10), can be re-written in the form

$$K\ell^{i\epsilon} =\mid K\ell^{i\epsilon} \mid e^{i\psi^*} \tag{11}$$

with the immediate interpretation that ψ^* is the phase angle of the complex quantity $K\ell^{i\epsilon}$; note too that $K\ell^{i\epsilon}$ has the same units MPa$\sqrt{\text{m}}$ as that of the conventional stress intensity factor in the bulk solid, as seen by inspection of (8).

If, instead of ℓ, the crack length a is now taken as the length scale for definition of the mode mix, then the associated phase angle ψ is defined by

$$\tan\,\psi = \frac{\sigma_{12}(x_1 = a)}{\sigma_{22}(x_1 = a)} = \frac{\text{Im}(Ka^{i\epsilon})}{\text{Re}(Ka^{i\epsilon})} \tag{12}$$

such that

$$Ka^{i\epsilon} =\mid Ka^{i\epsilon} \mid e^{i\psi} \tag{13}$$

The phase angles ψ^* and ψ are directly related by noting that

$$Ka^{i\epsilon} = K\ell^{i\epsilon}e^{i\epsilon\ln(a/\ell)} \tag{14}$$

and consequently

$$\psi = \psi^* + \epsilon\ln(\frac{a}{\ell}) \tag{15}$$

via (11) and (13). Typically, the difference between ψ^* and ψ is negligible since ϵ is small and there is a logarithmic dependence upon a/ℓ. In the present study we assume that the length scale ℓ for which the mode mix is important is on the order of the plastic zone size, r_p at the

tip of a mode I interfacial crack at fracture. Assume that $r_p = E\Gamma_I/(3\pi\sigma_y^2)$ where $E = 2.20$ GPa, $\sigma_y = 32$ MPa and the interfacial mode I toughness $\Gamma = 8.7$ Jm^{-2} (as measured later in this study from tests on a modified compact tension specimen). Consequently, we find that $\ell = r_p$ =2.0 μm.

The energy release rate G is related to the interfacial stress intensity factor K according to (Hutchinson and Suo, 1991)

$$E^*G = (1-\beta^2)(K_1^2 + K_2^2) \tag{16}$$

where the combined modulus E^* is related to the shear moduli μ_i, and $\kappa_i = 3 - 4\nu_i$, via

$$\frac{16}{E^*} = \frac{1+\kappa_1}{\mu_1} + \frac{1+\kappa_2}{\mu_2} \tag{17}$$

4.2.1. Interfacial crack embedded in the corner singular field

First consider the case where the interfacial crack is embedded within the corner singular field of intensity H. $Ka^{i\epsilon}$ must scale linearly with H, and dimensional analysis dictates that the connection formula between $Ka^{i\epsilon}$ and H is of the form

$$Ka^{i\epsilon} = dHa^{\lambda-0.5} \tag{18}$$

where the complex calibration factor $d = d_R + id_I$ is a function only of (α, β). The value of d has been obtained previously by Khaderi et al. (Khaderi et al., 2015) for the full range of (α, β), and we include in Table 1 the values of d for ($\alpha = -0.97$, $\beta = 0$) and for ($\alpha = -0.97$, $\beta = -0.16$) as taken from Khaderi et al. (Khaderi et al., 2015). Now make use of relations

(5) and (18) to write

$$\frac{K}{\tau^{\infty}\sqrt{h}} = (3.89 + i1.19)(a/h)^{0.10} \tag{19}$$

for the choice ($\alpha = -0.97$, $\beta = 0$) and

$$\frac{Ka^{i\epsilon}}{\tau^{\infty}\sqrt{h}} = (4.54 + i1.37)(a/h)^{0.15} \quad \text{and} \quad \epsilon = 0.0517 \tag{20}$$

for ($\alpha = -0.97$, $\beta = -0.16$). We note from (19) and (20) that the dependence of $\mid Ka^{i\epsilon} \mid$ upon crack length a is rather mild due to the small value of the exponent a/h. The expressions (19) and (20) are plotted in Fig. 7(a). By making use of (16), the energy release rate G versus crack length a is obtained and is shown in Fig. 7(b). Additionally, the phase angle ψ, based on the length scale a, is shown in Fig. 7(c): ψ equals 17.0° and 16.8° for $\beta = 0$ and $\beta = -0.16$, respectively. We conclude that a short crack at the interface-corner of the TAST specimen is predominantly loaded in mode I.

4.2.2. General case of an interfacial crack

Second, consider the more general case of an interfacial crack of arbitrary length a along the lower interface. A finite element analysis is performed on the entire specimen geometry of Fig. 5(a), and the value of K is determined by a domain integral method as an in-built subroutine within the ABAQUS program. The sensitivity of K and of phase angle ψ to a is plotted in Fig. 7(a) for $\alpha = -0.97$, with $\beta = 0$ or $\beta = -0.16$. At short crack lengths, $a/h < 0.1$, there is good agreement with the asymptotic solution of a short crack embedded within the corner singular field. When the crack extends beyond the corner singularity, the phase angle ψ increases with increasing a/h from $\psi = 17.0°$ (mode I dominated) to

$\psi = 90.0°$ (mode II limit). Consequently, at large values of a/h the crack tips approach each other from opposite ends of the specimen, and K becomes sensitive to a/h within the regime $3 < a/h < 6$; this behaviour is also evident in Fig. 5.

Recall that the observed fracture strength of the epoxy layer scales as $h^{-0.5}$ in Fig. 4, for $a/W = 0.2$ and 0.4 ($W = 50$ mm). This dependence is consistent with the prediction by a straightforward calculation of the energy release rate G for a semi-infinite crack along the lower interface of an infinite layer of adhesive, of height h, sandwiched between two rigid substrates (Martínez-Pañeda et al., 2020; Rice and Rosengren, 1968). The layer is of shear modulus μ_1 and Poisson ratio ν_1, and the upper substrate is displaced in a sliding direction with respect to the lower substrate by an amount $h\gamma$ where γ is the shear strain in the intact layer, upstream of the crack tip. Write $\tau^\infty = \mu_1\gamma$ as the shear stress on the layer upstream of the crack tip. Then the upstream strain energy density of the sandwich layer, per unit area, reads

$$W^u = \frac{1}{2}\frac{\tau^{\infty 2} h}{\mu_1} \tag{21}$$

while the downstream strain energy density W^D vanishes downstream of the crack tip. Consequently, the energy release rate is $G = W^u$. Upon equating G to the interfacial toughness Γ we find that the shear strength τ_c^∞ (upstream of the crack tip) is

$$\tau_c^\infty = \left(\frac{2\mu_1\Gamma}{h}\right)^{\frac{1}{2}} \tag{22}$$

Consequently, τ_c^∞ scales as $h^{-\frac{1}{2}}$, as observed in Fig. 4.

It remains to deduce the locus of interfacial toughness Γ as a function of phase angle ψ

(based on a) and ψ^* (based on $\ell = 2.0$ μm) from the TAST results of Figs. 3(b, c). An additional test is needed in order to obtain values for $\Gamma(\psi^*)$ for ψ^* small, that is close to mode I. To achieve this, fracture tests were performed on a modified version of compact tension test, as shown in Fig. 8. The same material combination was used on this sandwich specimen of thickness 25 mm; the adhesive layer thickness h was 5 mm and the initial crack length was 10 mm. All other relevant dimensions, and the load versus displacement response for 3 repeat tests, are given in the sketch of Fig. 8. A subsidiary ABAQUS calculation of the K-calibration revealed that the test is almost mode I in nature, with $\psi = 8.7^\circ$ and $\psi^* = -16.1^\circ$. Consequently, relation (16) provides $\Gamma(\psi^* = -16.1^\circ) = 8.7$ Jm^{-2}.

The fracture locii of $\Gamma(\psi)$ and $\Gamma(\psi^*)$ for the TAST specimens, and for the modified compact tension test, are shown in Fig. 9. Additional insight into the TAST specimens is obtained by reporting in Table 2 the interfacial K-calibration for the practical range of values of h/W, with $a/w = 0.20$ and 0.40, and for the choice $\alpha = -0.97$ and $\beta = -0.16$. Note that the phase angle ψ, based on a, ranges from 50° at $h/W = 0.26$ (and $a/W = 0.20$) to 87° at $h/W = 0.06$ (and $a/W = 0.40$) and the phase angle ψ^* (based on $\ell = 2.0$ μm) ranges from 25° to 60° with decreasing h/W. The phase angle ψ^* is shifted from that of ψ by approximately 27° upon making use of (15) with $\epsilon = 0.0517$ and $\ell = 2.0$ μm.

It is clear from Fig. 9(a) that, for a given value of a/W, the phase angle ψ^* (and likewise phase angle ψ in Fig. 9(b)) increases by approximately 20° with decreasing h/W, from $h/W = 0.26$ to $h/W = 0.06$. Over this range Γ has a minor sensitivity to ψ^* and to ψ. Thus, it is expected from (22), and from the more detailed evaluations in Table 2, that the shear strength scales as $h^{-\frac{1}{2}}$ in line with the measurement reported in Fig. 4(b).

5. Concluding Remarks

The current study provides a fracture mechanics for crack initiation from a sharp corner and for crack growth from a pre-existing flaw along the interface of a lap-joint in the form of a TAST specimen. The low value of interfacial toughness implies that a elastic analysis is adequate for our purposes. The low values of interfacial toughness, large elastic mismatch between adhesive layer and substrate, and the finite value of mismatch parameter β together lead to a large shift of approximately 27° in phase angle for an interfacial crack when the relevant length scale is shifted from crack length a to plastic zone size ℓ. More commonly, the shift in phase angle is only a few degrees for an interfacial crack in a sandwich layer, for example for a ceramic layer or a tough polymeric layer. The present study reveals that the phase angle ψ^* in the TAST specimens is on the order of 25° to 60° (depending upon the value of a/W and h/W). This implies that the test is mixed mode in nature, and is not a pure mode II fracture test.

Acknowledgment

This project has received funding from the Interreg 2 Seas programme 2014-2020 co-funded by the European Regional Development Fund under subsidy contract No 03-051. Additional support of Prof. Norman Fleck was provided by, the ERC project "Multi-phase Lattice Materials" (MULTILAT) under Grant No. 669764.

Appendix

Asymptotic analysis of stress distribution near a corner

The asymptotic solution for the stress and displacement fields near a bi-material corner is derived below. Consider the geometry shown in Fig. 5(a), and introduce both a Cartesian co-ordinate system (x, y) and a polar co-ordinate system (r, θ) centred on the corner. The location of any material point in the vicinity of the corner can also be stated in complex variable form as $z = x + iy = re^{i\theta}$. Introduce m as the index that identifies the material above $(m = 1)$ or below $(m = 2)$ the interface, with $\kappa_m = 3 - 4\nu_m$. Now write $()'$ as the derivative and $\bar{()}$ as the complex conjugate of any complex function, in the usual manner. Then, upon following Muskhelishvili (Muskhelishvili, 1955), the stress and displacements in materials 1 and 2 can be expressed in terms of complex potentials $\Phi_{(m)}(z)$ and $\Omega_{(m)}(z)$ as

$$\sigma_{\theta\theta}^{(m)} - i\sigma_{r\theta}^{(m)} = \bar{\Phi}'_{(m)}(\bar{z}) + \Phi'_{(m)}(z) + \bar{z}\bar{\Phi}''_{(m)}(\bar{z}) + z^{-1}\bar{z}\bar{\Omega}'_{(m)}(\bar{z}) \tag{23}$$

$$\sigma_{rr}^{(m)} + i\sigma_{r\theta}^{(m)} = \bar{\Phi}'_{(m)}(\bar{z}) + \Phi'_{(m)}(z) - \bar{z}\bar{\Phi}''_{(m)}(\bar{z}) - z^{-1}\bar{z}\bar{\Omega}'_{(m)}(\bar{z}) \tag{24}$$

$$u_r^{(m)} + iu_\theta^{(m)} = (2\mu_m)^{-1}e^{-i\theta}\big(\kappa_m\Phi_{(m)}(z) - z\bar{\Phi}'_{(m)}(\bar{z}) - \bar{\Omega}_{(m)}(\bar{z})\big) \tag{25}$$

The complex potentials $\Phi_{(m)}(z)$ and $\Omega_{(m)}(z)$ have the following asymptotic form as $z \to 0$, (see for example, (England, 1971; Stern et al., 1976; Carpenter and Byers, 1987)),

$$\Phi_1 = Az^\lambda, \quad \Omega_1 = Bz^\lambda \tag{26}$$

$$\Phi_2 = Cz^\lambda, \quad \Omega_1 = Dz^\lambda \tag{27}$$

where (A,B,C,D) are complex coefficients to be determined by satisfaction of the appropriate boundary conditions:

For the corner singularity problem, the following boundary conditions need to be satisfied

$$\sigma^{(1)}_{\theta\theta} - i\sigma^{(1)}_{r\theta} = \sigma^{(2)}_{\theta\theta} - i\sigma^{(2)}_{r\theta} \qquad \text{along } \theta = 0 \tag{28}$$

$$u^{(1)}_r + iu^{(1)}_\theta = u^{(2)}_r + iu^{(2)}_\theta \qquad \text{along } \theta = 0 \tag{29}$$

$$\sigma^{(1)}_{\theta\theta} - i\sigma^{(1)}_{r\theta} = 0 \qquad \text{along } \theta = \frac{\pi}{2} \tag{30}$$

$$\sigma^{(2)}_{\theta\theta} - i\sigma^{(2)}_{r\theta} = 0 \qquad \text{along } \theta = -\pi \tag{31}$$

Hence,

$$A + \lambda\bar{A} + \bar{B} - C - \lambda\bar{C} - \bar{D} = 0 \tag{32}$$

$$\kappa_1 A - \lambda\bar{A} - \bar{B} - \mu(\kappa_2 C - \lambda\bar{C} - \bar{D}) = 0 \tag{33}$$

$$Ae^{i\pi\lambda} - \lambda\bar{A} + \bar{B} = 0 \tag{34}$$

$$Ce^{i2\pi\lambda} + \lambda\bar{C} + \bar{D} = 0 \tag{35}$$

where $\mu = \mu_1/\mu_2$, $A = A_R + iA_I$, and likewise for B, C, and D. Upon rewriting (32) and (33) as a function of A_R and A_I only, and equating the determinant of the coefficient matrix for A_R and A_I to zero, the charactristic equation is obtained as $F(\lambda) = 0$, where

$$F(\lambda) = \{\big[4\big(\kappa_1^2 - 4\lambda^2 + 1\big) + 8\kappa_1 \cos(\pi\lambda)\big]\sin^2(\pi\lambda)$$

$$- 2\mu^2\big[\big(\cos(\pi\lambda) + 2\lambda^2 - 1\big)(4\kappa_2\cos^2(\pi\lambda) + (\kappa_2 - 1)^2\big)\big]$$

$$-4\mu\big[(\kappa_2{-}1)\big(4\lambda^2\sin^2(\pi\lambda){-}(\kappa_1{-}1)\cos^2(\pi\lambda)\big){+}(\kappa_1\kappa_2{+}1)\big(1{-}\sin(2\pi\lambda)\sin(\pi\lambda)\big){-}\kappa_1{-}\kappa_2\big]\}/\{4\sin^2(\pi\lambda)\} \tag{36}$$

References

Akisanya, A., Fleck, N., 1997. Interfacial cracking from the freeedge of a long bi-material strip. International Journal of Solids and Structures 34, 1645–1665.

Bikerman, J.J., 2013. The science of adhesive joints. Elsevier.

Bogy, D., 1970. On the problem of edge-bonded elastic quarter-planes loaded at the boundary. International Journal of Solids and Structures 6, 1287–1313.

Bogy, D.B., 1968. Edge-bonded dissimilar orthogonal elastic wedges under normal and shear loading .

Carpenter, W.C., Byers, C., 1987. A path independent integral for computing stress intensities for v-notched cracks in a bi-material. International Journal of Fracture 35, 245–268.

Chiu, W., Jones, R., 1992. A numerical study of adhesively bonded lap joints. International Journal of Adhesion and Adhesives 12, 219–225.

Ding, S., Meekisho, L., Kumosa, M., 1994. Analysis of stress singular fields at a bimaterial wedge corner. Engineering fracture mechanics 49, 569–585.

Dundurs, J., 1969. Edge-bonded dissimilar orthogonal elastic wedges under normla and shear loading. Journal of Applied Mechanics 36, 650–652.

England, A., 1971. On stress singularities in linear elasticity. International Journal of Engineering Science 9, 571–585.

Gradin, A., 1982. A fracture criterion for edge-bonded bimaterial bodies. Journal of Composite Materials 16, 448–456.

Hattori, T., Sakata, S., Hatsuda, T., Murakami, G., 1988. A stress singularity parameter approach for evaluating adhesive strength. JSME International Journal. Ser. 1, Solid Mechanics, Strength of Materials 31, 718–723.

Hutchinson, J.W., Suo, Z., 1991. Mixed Mode Cracking in Layered Materials. Advances in Applied Mechanics 29, 63–191.

Kassapoglou, C., Adelmann, J., 1992. Kgr-1 thick adherend specimen evaluation for the determination of adhesive mechanical properties. SAMPE quarterly 24, 19–27.

Khaderi, S., Fleck, N., Arzt, E., McMeeking, R., 2015. Detachment of an adhered micropillar from a dissimilar substrate. Journal of the Mechanics and Physics of Solids 75, 159–183.

Knésl, Z., Klusák, J., Náhlík, L., 2007. Crack initiation criteria for singular stress concentrations, part i: a universal assessment of singular stress concentrations. Engineering mechanics 14, 399–408.

Koguchi, H., Inoue, T., Yada, T., 1996. Stress singularity in three-phase bonded structure .

Krieger, R.B., 1975. Stiffness characteristics of structural adhesives for stress analysis in hostile environment, in: Society for the Advancement of Material and Process Engineering, National Technical Conference, 7 th, Albuquerque, N. Mex, p. 1975.

Lang, T.P., Mallick, P., 1998. Effect of spew geometry on stresses in single lap adhesive joints. International Journal of Adhesion and adhesives 18, 167–177.

Maloney, K., Fleck, N., 2018. Damage tolerance of an architected adhesive joint. International Journal of Solids and Structures 132, 9–19.

Martínez-Pañeda, E., Cuesta, I.I., Fleck, N.A., 2020. Mode ii fracture of an elastic-plastic sandwich layer. Journal of Applied Mechanics 87.

Munz, D., Yang, Y., 1992. Stress singularities at the interface in bonded dissimilar materials under mechanical and thermal loading. ATJAM 59, 857–861.

Muskhelishvili, N., 1955. Some basic problems of the mathematical theory of elasticity. Bull. Amer. Math. Soc 61, 445–447.

Pageau, S.S., Biggers, S.B., 1995. Finite element evaluation of free-edge singular stress fields in anisotropic materials. International Journal for Numerical Methods in Engineering 38, 2225–2239.

Pageau, S.S., Joseph, P.F., Biggers, S.B., 1995. Finite element analysis of anisotropic materials with singular inplane stress fields. International Journal of Solids and Structures 32, 571–591.

Pandini, S., Pegoretti, A., 2008. Time, temperature, and strain effects on viscoelastic poisson's ratio of epoxy resins. Polymer Engineering & Science 48, 1434–1441.

Possart, W., Brede, M., 2019. Adhesive Joints: Ageing and Durability of Epoxies and Polyurethanes. John Wiley & Sons.

Reedy, E., 1993. Asymptotic interface corner solutions for butt tensile joints. International Journal of Solids and Structures 30, 767–777.

Reedy, E., Guess, T., 1993. Comparison of butt tensile strength data with interface corner

stress intensity factor prediction. International Journal of Solids and Structures 30, 2929–2936.

Reedy, E., Guess, T., 1995. Butt joint tensile strength: interface corner stress intensity factor prediction. Journal of Adhesion Science and Technology 9, 237–251.

Reedy, E., Guess, T., 1996. Interface corner stress states: plasticity effects. International Journal of Fracture 81, 269–282.

Reedy, E., Guess, T., 1997. Interface corner failure analysis of joint strength: effect of adherend stiffness. International Journal of Fracture 88, 305–314.

Rice, J.R., Rosengren, G.F., 1968. Plane strain deformation near a crack tip in a power-law hardening material. Journal of the Mechanics and Physics of Solids 16, 1–12.

Saeedifar, M., Saleh, M.N., De Freitas, S.T., Zarouchas, D., 2019. Damage characterization of adhesively-bonded bi-material joints using acoustic emission. Composites Part B: Engineering 176, 107356.

Saleh, M.N., Saeedifar, M., Zarouchas, D., De Freitas, S.T., 2020. Stress analysis of double-lap bi-material joints bonded with thick adhesive. International Journal of Adhesion and Adhesives 97, 102480.

Stern, M., Becker, E., Dunham, R., 1976. A contour integral computation of mixed-mode stress intensity factors. International Journal of Fracture 12, 359–368.

Williams, M., 1952. Stress singularities resulting from various boundary conditions in angular corners of plates in extension. Journal of Applied Mechanics 19, 526–528.

Table 1: Corner singularity parameters for the choice $\alpha = -0.97$, and $\beta = 0$, -0.16.

$\beta = 0$					$\beta = -0.16$				
λ	b	f_{12}	d_R	d_I	λ	b	f_{12}	d_R	d_I
0.60	1.47	0.51	2.65	0.81	0.65	1.78	0.42	2.55	0.77

Table 2: K-Calibration for TAST specimen.

	$\frac{\mathrm{Re}(Ka^{i\epsilon})}{\tau^\infty\sqrt{h}}$	$\frac{\mathrm{Im}(Ka^{i\epsilon})}{\tau^\infty\sqrt{h}}$	ψ (°)	$\frac{\mathrm{Re}(K\ell^{i\epsilon})}{\tau^\infty\sqrt{h}}$	$\frac{\mathrm{Im}(K\ell^{i\epsilon})}{\tau^\infty\sqrt{h}}$	ψ^* (°)
h/W	$a/W = 0.20$					
0.06	0.91	3.16	73.9	2.15	2.50	49.3
0.10	0.89	2.73	71.9	1.96	2.11	47.1
0.16	1.05	2.30	65.4	1.92	1.64	40.6
0.20	1.21	2.06	59.6	1.97	1.37	34.9
0.26	1.50	1.80	50.3	2.12	1.01	25.5
	$a/W = 0.40$					
0.06	0.24	3.57	86.1	1.81	3.08	59.5
0.10	0.22	3.20	86.1	1.61	2.76	59.5
0.16	0.37	2.88	82.7	1.62	2.41	56.1
0.20	0.51	2.72	79.4	1.68	2.20	52.7
0.26	0.76	2.52	73.2	1.81	1.91	46.6

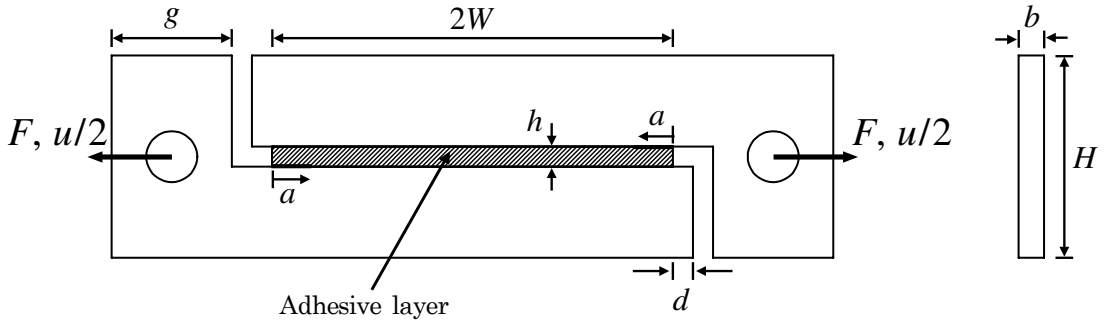

Figure 1: Modified TAST specimen. $2W = 100$ mm; $h = 3 - 13$ mm; $H = 50.4$ mm; $g = 30$ mm; $a = 0 - 20$ mm; $d = 5$; $b = 6.35$.

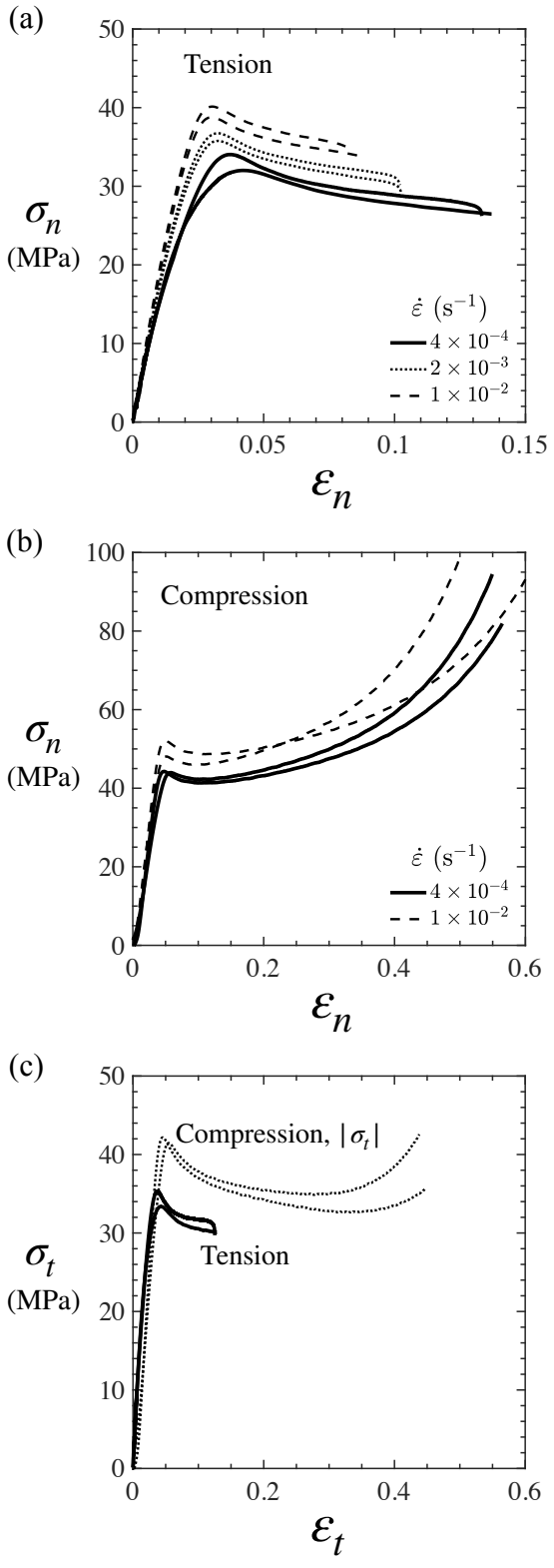

Figure 2: Uniaxial response of the epoxy in bulk form. (a) Nominal tensile response; (b) Nominal compression response; (c) True stress σ_t versus true strain ε_t curves in tension and compression, at $\dot{\varepsilon} = 4 \times 10^{-4}\ s^{-1}$.

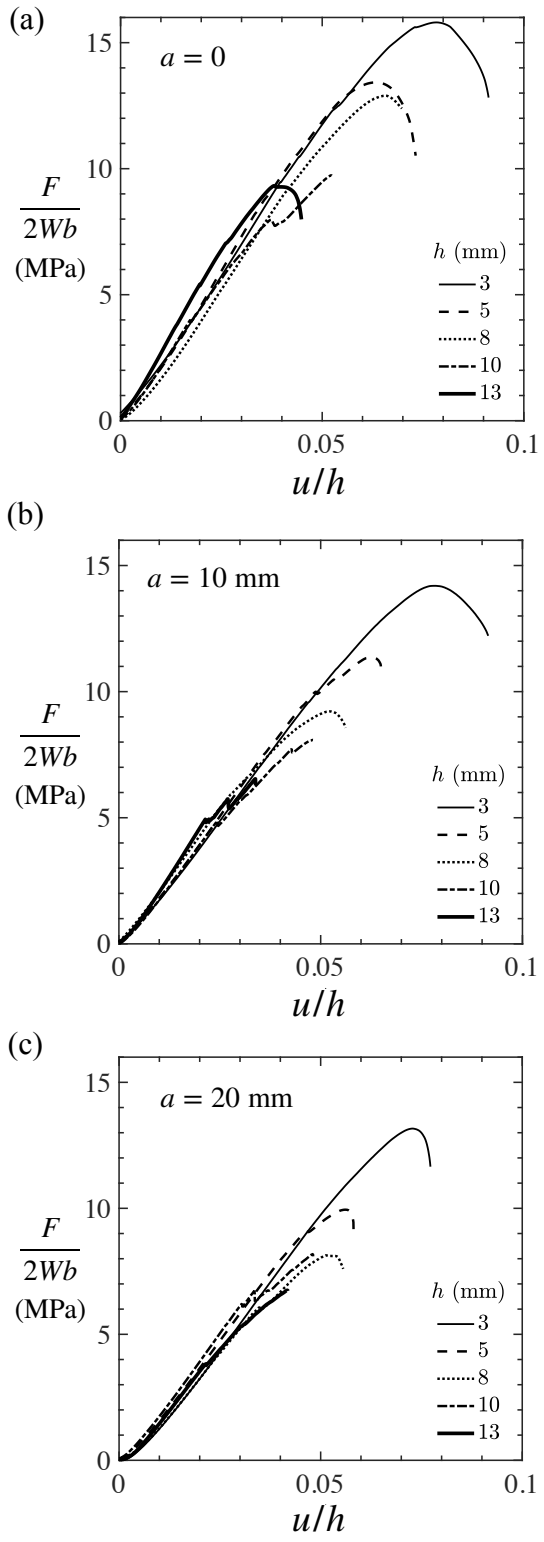

Figure 3: Gross-section shear stress ($F/2Wb$) versus average shear strain u/h of the adhesive layer, for pre-crack length (a) $a = 0$, (b) $a = 10$ mm, and (c) $a = 20$ mm.

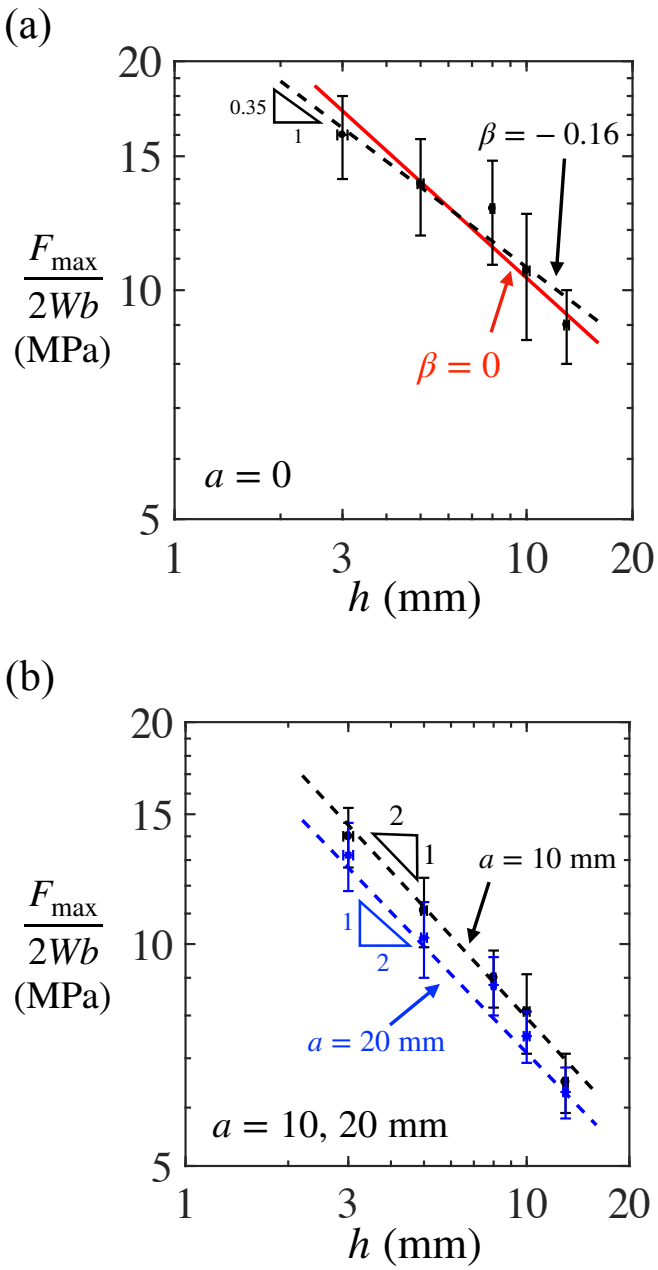

Figure 4: Effect of adhesive thickness h on failure strength ($\tau_c^{\infty} = F_{\max}/2Wb$) of TAST specimens for (a) no pre-crack, $a = 0$, and (b) a pre-crack of length $a = 10$ mm, and 20 mm.

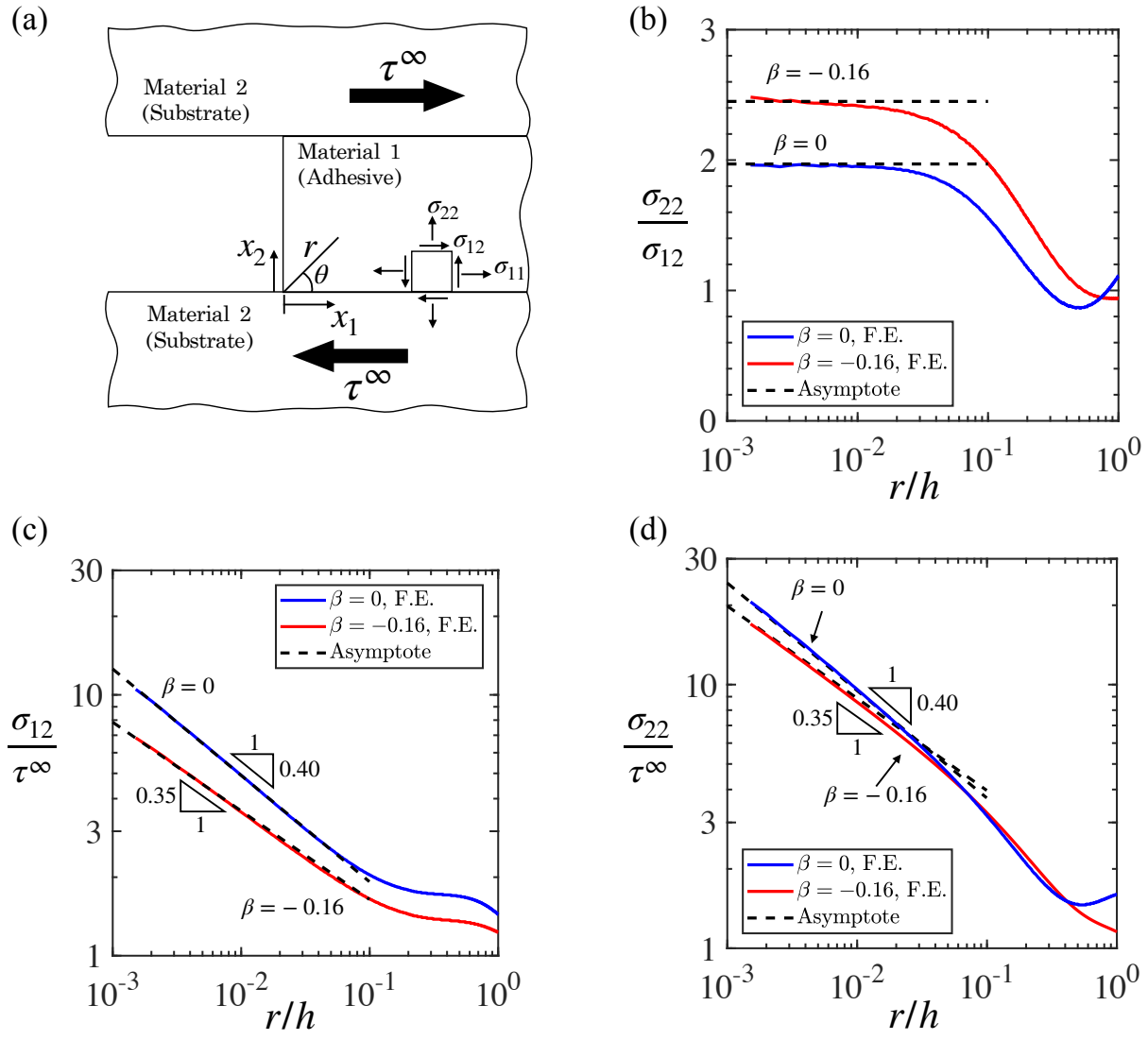

Figure 5: The traction (σ_{12}, σ_{22}) along the interface associated with the corner singularity. (a) geometry and local co-ordinate system; (b) σ_{22}/σ_{12}, (c) σ_{12}/τ^∞ , and (d)σ_{12}/τ^∞ versus r/h. Here, $\tau^\infty = F/2Wb$. The corner singularity asymptotic solution is dominant for $r/h < 0.1$.

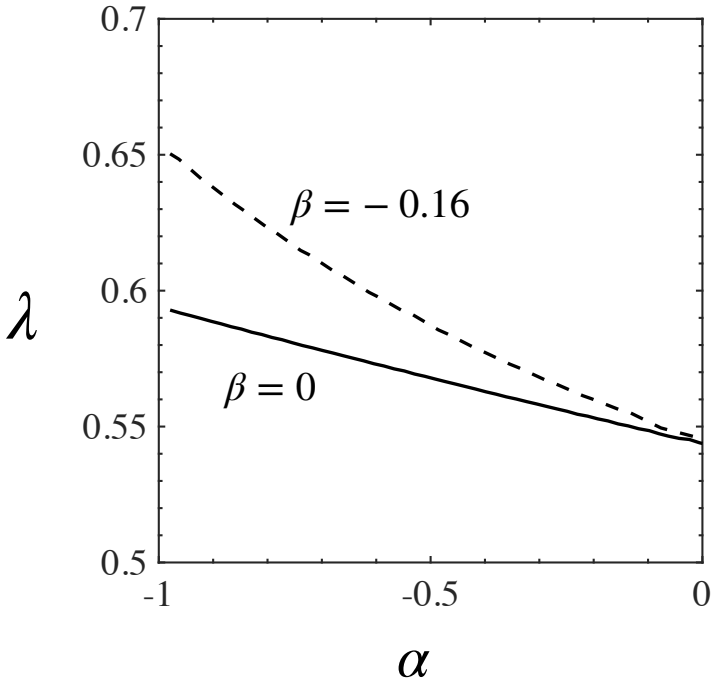

Figure 6: Effect of Dundurs parameters (α and β) on order λ of the 90° corner singularity.

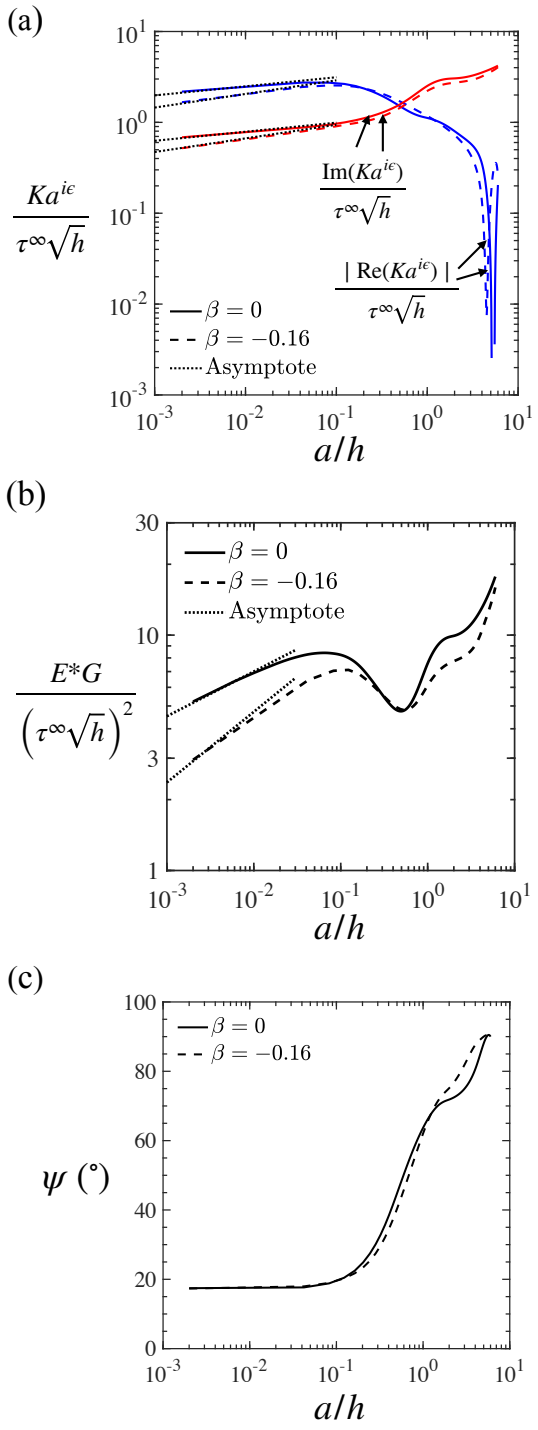

Figure 7: (a) Interfacial stress intensity factor versus a/h for $\alpha = -0.97$ and (β = 0, -0.16), and for $h/W = 0.10$, (b) Energy release rate versus a/h, (c) Phase angle ψ (based on a) versus a/h. At short crack lengths, $a/h < 0.1$, there is good agreement between the full FE solution and the asymptotic solution of a short crack embedded within the corner singular field.

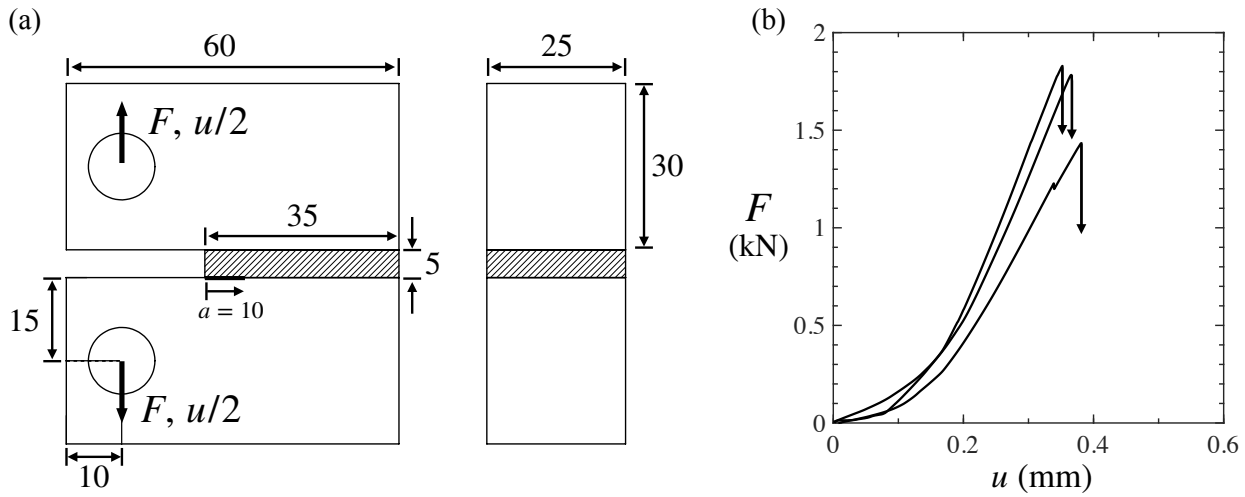

Figure 8: (a) Sketch of the modified compact tension specimens. All dimensions are in mm. (b) Force versus displacement curve of the compact tension test for three nominally identical specimens.

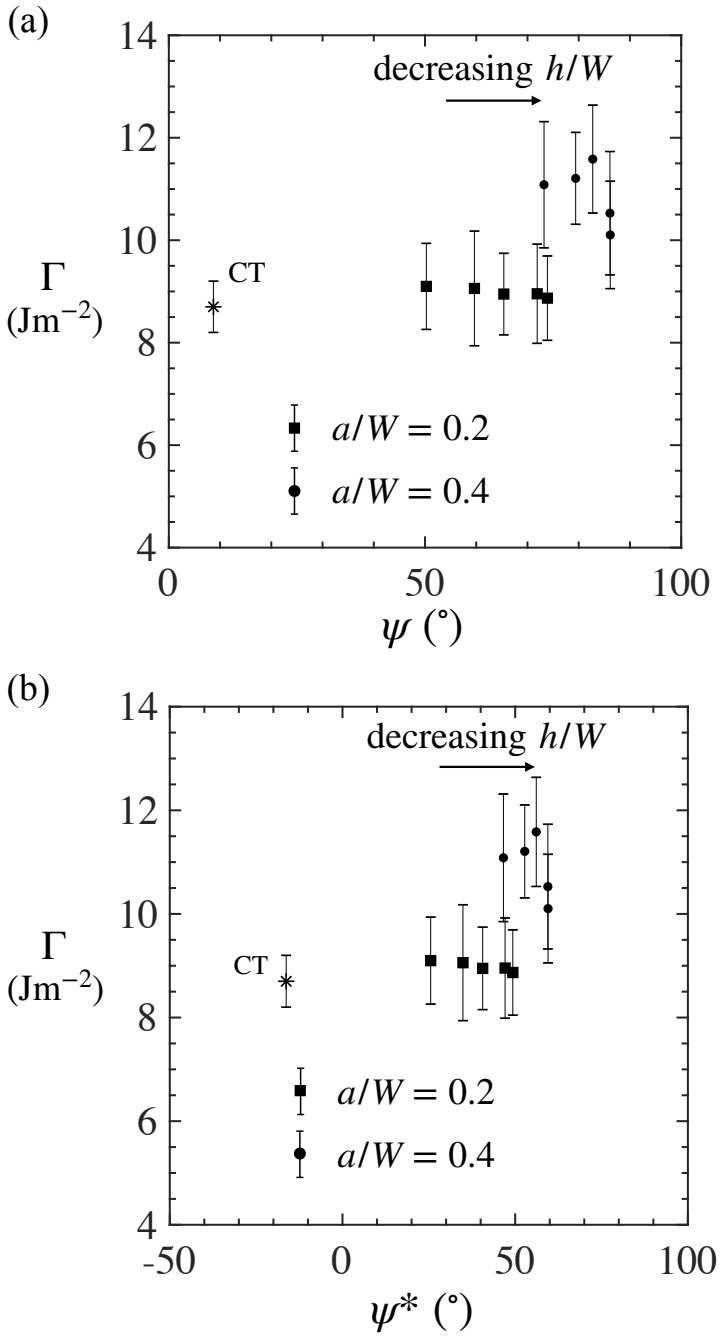

Figure 9: (a) Interface toughness versus ψ (based on a); (b) Interface toughness versus ψ^* (based on ℓ), obtained from TAST specimens and compact tension (CT) test. When the relevant length scale is shifted from crack length a to the plastic zone size ℓ, the phase angle shifts by 27°.